Sheffield Hallam University

Analyzing the engineering feasibility of the direct fusion drive

JAIN, Yuvraj and KAKADE, Priyanka <http://orcid.org/0000-0002-0131-391X>

Available from Sheffield Hallam University Research Archive (SHURA) at:

https://shura.shu.ac.uk/31475/

This document is the Published Version [VoR]

Citation:

JAIN, Yuvraj and KAKADE, Priyanka (2023). Analyzing the engineering feasibility of the direct fusion drive. Acta Astronautica, 206, 57-71. [Article]

Copyright and re-use policy

See http://shura.shu.ac.uk/information.html

Sheffield Hallam University Research Archive
http://shura.shu.ac.uk

Acta Astronautica 206 (2023) 57–71

Contents lists available at ScienceDirect

Acta Astronautica

journal homepage: www.elsevier.com/locate/actaastro

Research paper

Analyzing the engineering feasibility of the direct fusion drive

Yuvraj Jain [a,1], Priyanka Desai Kakade [b,2,*]

[a] Department of Electronics and Communication Engineering, Manipal Institute of Technology, Manipal Academy of Higher Education, Manipal, 576104, Karnataka, India

[b] Department of Engineering and Mathematics, Sheffield Hallam University, Sheaf Building, City Campus, Sheffield, S1 1WB, United Kingdom

ARTICLE INFO

Keywords:
Nuclear fusion
Propulsion
FRC
Engineering feasibility
Deuterium
Helium-3

ABSTRACT

The Direct Fusion Drive (DFD) and its terrestrial counterpart, the Princeton Field Reversed Configuration (PFRC) reactor, have seen significant developments in the past decade. Various groups conducted detailed research on the required specifications of the engine and associated technology for power delivery to onboard avionics and payloads. Multiple studies have also addressed the thrust generation mechanism using empirical specific power scaling relations and plasma flow simulations. Recent studies have designed spacecraft for missions to Earth's second Lagrange point, Mars, transneptunian bodies like Pluto, and the neighboring star systems Alpha Centauri A and B. However, significant work is needed to design the engine components in detail using scientific scaling relations and ab inito calculations to develop the physical systems for prototyping and testing. After critically analyzing the reference design of the DFD and the underlying fusion reactor, this paper addresses the technological gaps and suggests avenues to improve specifications toward targets outlined in previous studies while considering costs. Further, the authors present a prototype engine and magnetohydrodynamic power conversion system design to study the engineering hurdles relevant to the practical implementation of the DFD.

1. Introduction

The Direct Fusion Drive (DFD) is a conceptual nuclear fusion-based rocket propulsion engine. Building on the Princeton Field Reversed Configuration (PFRC) fusion reactor design, the DFD modifies the structure to include a magnetic nozzle and a gas box. The conceptual design simultaneously produces thrust and electrical power [1].

The core concept is exceedingly simple in engineering complexity and reactor design. Two solenoids generate a linear axial magnetic field modulated by isolated copper and superconducting tape rings. A rotating magnetic field creates an azimuthal current in the injected gas, ionizing the gas and canceling the applied axial field. The produced toroidal plasma forms a region of no magnetic field at its boundary, a separatrix, beyond which a layer of low-temperature plasma exists. The DFD exploits the low-temperature scrape-off layer (SOL) by injecting propellant and exhausting it from a magnetic nozzle after heating it [2]. Fig. 1 shows the DFD's configuration from [2].

On the other hand, the plasma dynamics of the device are rich and complex. Examples include stochastic ion trajectories [3], internal tilt susceptibility, independent species behavior, and a detailed internal plasma structure [4]. A Rotating Magnetic Field (RMF) current drive generates an odd parity time-varying magnetic field about the mid-plane of the device. Due to the alternating nature of the RMF direction in space, the PFRC boasts improved plasma confinement and efficient conversion of input energy to electron thermal energy [5]. In theory, odd parity RMF current drive and non-Maxwellian ion energy distribution enable the device to burn aneutronic fuels such as D – 3He while minimizing neutron flux from D – D fusion in the background [6,7].

The DFD concept represents a significant advancement in rocket propulsion due to its capability to deliver a specific impulse of tens of thousands of seconds and its high specific power. Trajectory simulations indicate that it could significantly reduce transit time and required propellant mass while maximizing payload mass in various scenarios, such as asteroid deflection missions [8] or missions to Pluto [9]. The DFD can also deliver high exhaust velocities resulting in ΔV of the order of 100 km/s, which enables nearly straight-line trajectories instead of hyperbolic transfer orbits [9]. Multiple upcoming space exploration goals, such as crewed exploration of Mars and robotic exploration of the outer solar system, stand to benefit from these specifications [10]. Furthermore, a legacy of two decades of Field Reversed Configuration

* Corresponding author.
E-mail addresses: yuvraj.jain1@learner.manipal.edu (Y. Jain), P.D.Kakade@shu.ac.uk (P.D. Kakade).
URLs: https://www.linkedin.com/in/yuvraj-jain-1a8a591b7/ (Y. Jain), https://www.scopus.com/authid/detail.uri?authorId=57205023532 (P.D. Kakade).
[1] Propulsion Engineer and Researcher at thrustMIT, Manipal, Karnataka, India.
[2] Lecturer at Sheffield Hallam University, United Kingdom. Previously, Associate Professor at Manipal Institute of Technology, Manipal, Karnataka, India.

https://doi.org/10.1016/j.actaastro.2023.02.011
Received 12 March 2022; Received in revised form 10 January 2023; Accepted 6 February 2023
Available online 10 February 2023
0094-5765/© 2023 The Author(s). Published by Elsevier Ltd on behalf of IAA. This is an open access article under the CC BY-NC-ND license (http://creativecommons.org/licenses/by-nc-nd/4.0/).

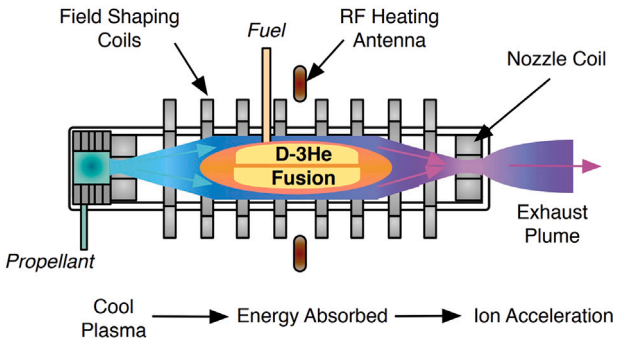

Fig. 1. Schematic Diagram of the Direct Fusion Drive (DFD). The figure illustrates the internal subsystems in the DFD and shows the mechanisms used to heat the plasma and generate thrust.
Source: Reproduced without modification from [2] with permission.

research and conceptual simplicity implies that a realizable DFD relies on current technology, albeit with some subsystems leveraging promising prototype technologies [11]. Its potential has led to active research with assistance and funding from various governmental agencies such as the US Department of Energy (DOE) and the National Aeronautics and Astronautics Administration (NASA) [11].

2. Current status and technology gaps

A fully-realized Field Reversed Configuration fusion reactor is the basis of the Direct Fusion Drive. Hence, it is necessary to analyze the current status of Field Reversed Configuration (FRC) reactor technology. The PFRC – 2 prototype targets ion heating up to 1 KeV, commissioned in 2011. Publications show that it has also achieved electron temperatures of 300 eV to date [11].

Before testing a full-scale reactor, four more prototypes, designated PFRC – 3A, PFRC – 3B, PFRC – P, and PFRC – 4, are slated to be developed under an expansive timeline. The design process for the PFRC – 3 series and PFRC – 4 began in the early 2010s and continues. The PFRC – 3A aims to demonstrate ion heating above 5 KeV, with the PFRC – 3B switching to D – 3He fuel and confirming fusion reactions. The PFRC – 4 aims to produce net power output from the fusion reaction for power generation. Born out of a proposal to NASA's Deep Space Rapid Transit Institute, the PFRC – P is meant to act as a testbed for propulsion-specific studies [11]. Originally envisioned in 2002, the first development timeline for the DFD was published in [10] and anticipated a flight-ready engine by 2024. A recent report has pushed the flight-ready engine tests to 2040 [11] due to the numerous engineering hurdles [12] and the general lack of funding for developing the prototypes beyond the PFRC – 2.

Various technology areas have significantly advanced since the PFRC – 1 [13]. However, the requirement for high-power, continuous-wave radio frequency (RF) sources remains a pressing concern. The screening effect of the electrons causes a significant loss in the heating efficiency of the rotating magnetic field [14]. The PFRC – 3 series and PFRC – 4 require significantly higher power RF sources [6] to compensate for current screening losses and achieve target plasma density and heating requirements. E–class switching amplifiers may provide one avenue to achieve the required RF power. However, studies have only considered 10 kW solid-state systems [11], while future prototypes require RF systems capable of providing at least 1 MW [6]. The 2019 DFD reference design shows that the plasma loses 40% of the fusion power as radiation, with only 22% of the generated power recirculating back to the RF systems [11]. [15] precludes the possibility of plasma self-heating, forcing the DFD to increase the RF recirculation power to ensure a constant plasma temperature. Hence, a DFD needs more input RF power than projections made for the PFRC. Any mechanism removing power from the FRC plasma, such as ion deceleration using the RMF [16], negatively affects the device's thrusting performance.

Further, the PFRC – 3 series and later devices in the development timeline require an overhaul of the passive superconducting flux conserver system to make sustained operations possible [17]. Another issue is that the neutron flux due to D – D side fusion reactions is estimated to be 6.1×10^{16} per second [18]. While the neutron flux power as a fraction of the total fusion power remains less than one percent, a shielding system is still necessary. For space-based applications, the weight of the underlying FRC reactor is critical. A recent study found that a minimum of 18.4 cm of shielding is required to meet the least conservative target of a lifetime neutron irradiance of 2×10^{18} per cm^2 of the superconducting flux conservers operating at liquid nitrogen temperature [18]. These results verified predictions made earlier in the scientific literature that neutron shielding can account for 22 to 66% of the DFD dry mass in various configurations for different applications [1,8,10,12,19]. The superconducting solenoids dominate the rest of the mass of the device [9,11,17].

Additionally, the neutron shield also doubles as a heat exchanger to drive a turbine to generate the electrical output of the reactor, complicating its design. The engineering constraints placed on the material used for the shield, aside from the neutron scattering cross-section requirement, include low electrical conductivity, ability to withstand thermal stresses, opacity to X-ray radiation, ability to reflect cyclotron radiation, and low blackbody emissivity [18]. [18] also concluded that no currently available engineering material satisfies all conditions and the best compromise was a hexagonal boron nitride and lithium hydride composite structure. This neutron shield is 2.7 tons for a practical 1 MW fusion power reactor and costs more than $ 2.48 million, assuming the least conservative neutron flux output. In contrast, [11] suggests a high-temperature superconducting flux conserver operating at 20 K to improve the superconductor's neutron flux tolerance, which results in shielding masses falling to 160 kg of lithium hydride, around 12% of the 1 MW reference engine's mass. For a short-term mission, [11] recommends removing the neutron shield to improve the engine's specific power. These findings clearly illustrate the need to reduce or eliminate neutron shielding mass to enhance the engine's specific power and lower the design's complexity.

The SOL dynamics are the final aspect of the underlying FRC technology discussed here. As illustrated in Fig. 1, many processes coincide in the SOL surrounding the burning plasma. Until recently, the DFD design utilized deuterium gas as reaction mass to augment the thrust generated by the device. However, recent studies have favored hydrogen gas for reaction mass [20]. The scientific literature provides no reasoning for selecting these gases for thrust augmentation in both cases. Experimental results in [11] show that a heated FRC significantly interacts with the plasma flow in the SOL to the point of overwhelming the SOL with its material blow-off. The effect of this blow-off and the significant reaction mass flow rate in the SOL on the neutral beam fuel injectors is unknown. The lack of plasma contamination studies to address the consequences of the substantial gas flow rate of hydrogen or deuterium (on the order of g/s) [2] around the burning plasma is also concerning. The SOL properties also have implications for the RF subsystem. A dense plasma sheath around the burning plasma in the DFD further exacerbates the RF shielding problem [14], leading the DFD to require even more RF power during operation.

Having addressed the underlying FRC technology, the authors now focus on DFD research. Fig. 2 illustrates the latest Computer-Aided-Design (CAD) of the propulsion concept from [17]. Initially proposed in 2002 [17], the DFD has evolved alongside the PFRC – 2 [1]. Aside from trajectory simulations for conceptual missions, there is a significant body of work on thrust prediction using 2D plasma simulations [2] and power generation for spacecraft systems [21]. Publications include system diagrams for the DFD and required specifications for conceptual missions. The system diagram is reproduced in Fig. 3 from [11] for context.

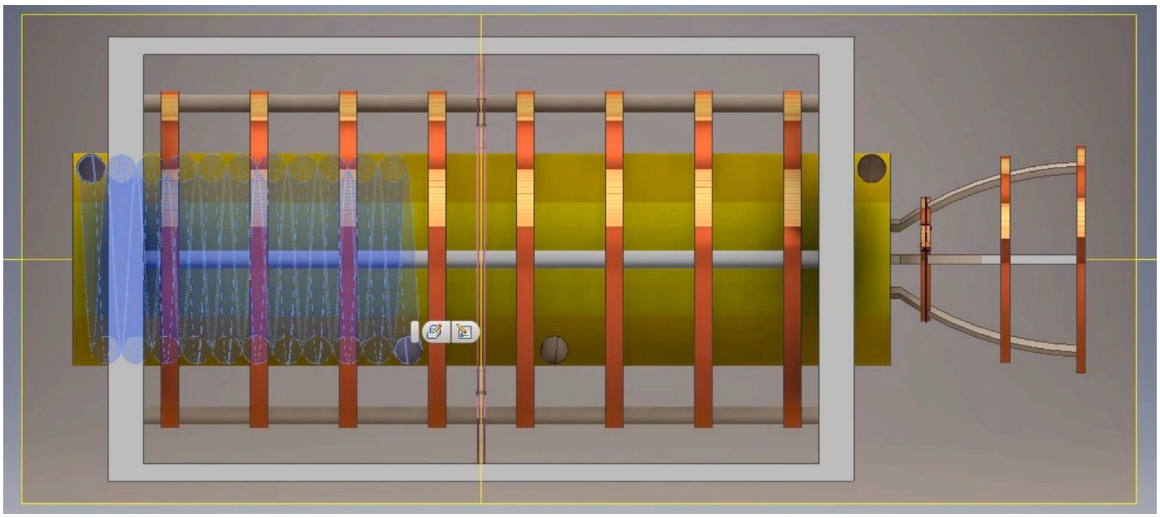

Fig. 2. A Computer Aided-Design (CAD) of the DFD. The helical coil highlighted in blue is the cooling channel embedded in the neutron shield. The copper-colored rings are the superconducting active flux conservers structurally supported by rods. The gray outer box is the engine chassis. Note the absence of detail regarding structural and cryostat design. (For interpretation of the references to color in this figure legend, the reader is referred to the web version of this article.)
Source: Reproduced without modification from [17] with permission.

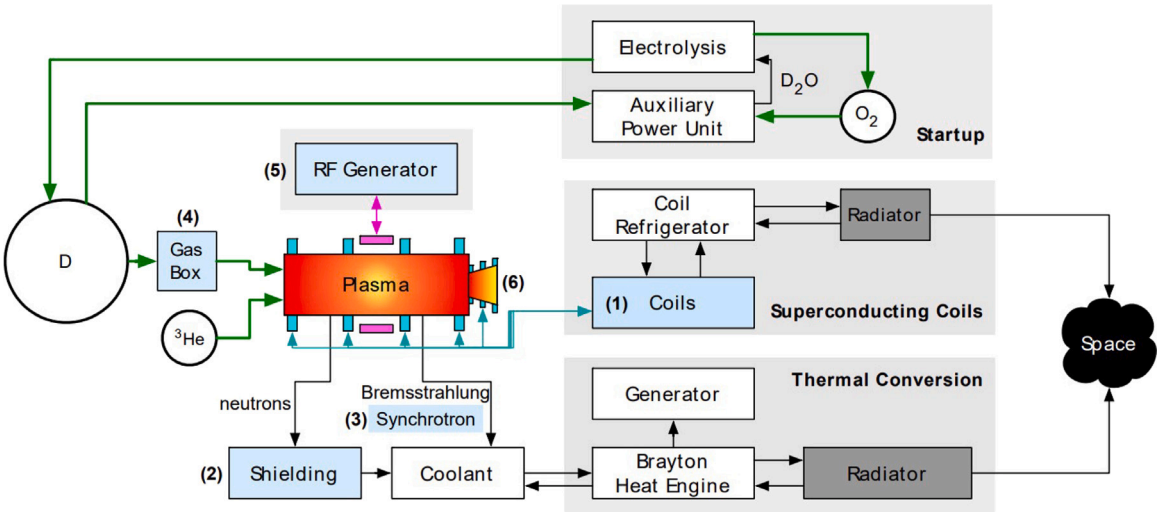

Fig. 3. DFD Systems Diagram. The figure depicts the various internal and external subsystems required to operate a DFD. Note the significance of the HTS Coil subsystem and the Power Recycling subsystem in DFD operation. The gray boxes group related subsystems together for easier understanding.
Source: Reproduced without modification from [11] with permission.

Two NASA NIAC (NASA Innovative Advanced Concept) reports in 2016 and 2019 consolidate and summarize the evolution of the design [17]. The 2019 report also details a reference DFD design of 1 MW and 10 MW fusion power engines [11]. Fig. 3 shows that the critical systems required to realize the DFD are the active superconducting flux conservers and the electrical power generation system.

The authors first consider the active superconducting flux conserver design, a subject covered in detail in [11]. The report includes low-temperature superconductors (LTS) and high-temperature superconductors (HTS). The design is optimized based on the mass of the flux conservers and the cryocooler mass taken together, with the cryocooler mass factored in using empirical scaling laws. The analysis includes the improved operating margins and irradiation tolerances from operating the HTS solenoids at a lower temperature [22].

Considering the 1,136 kA azimuthal current in the 40 cm, 1.784 T flux conserver from [11], the selected LTS material (SuperCon NbTi wire at an operating current of 528 A) with a diameter of 0.1 cm and HTS material (Superpower SCS12050 tape at an operating current of 1030 A) with a thickness of 0.01 cm yield superconducting pancake thicknesses of 107.57 cm and 11.03 cm respectively, significantly different from the values provided in [11]. This calculation finds the radial thickness by dividing the azimuthal current by the operating current, then multiplying it by the thickness of the material, assuming a 100% packing fraction. The pancakes' radial thickness significantly affects the design and mass of the cryostat, as shown in later sections. However, while there are numerous reports of calculated magnet specifications, no previous DFD design has explicitly included the effect of this parameter on the structural design. The 2019 report considers that HTS material is more competitive if the thickness of the tape substrate approaches 30 μm [11]. Results in [23] show that commercial HTS tape has achieved that thickness. However, [23] also reports advances in the REBCO layer fabrication, significantly improving the critical tape current from the value considered in [11] during magnet design.

The second subject of discussion is the thermal power conversion system, studied in detail by [17]. Radiation emitted from the FRC is incident on the neutron shield with helical or axial channels, which carry fluid to transfer heat to a Brayton power conversion cycle. The design

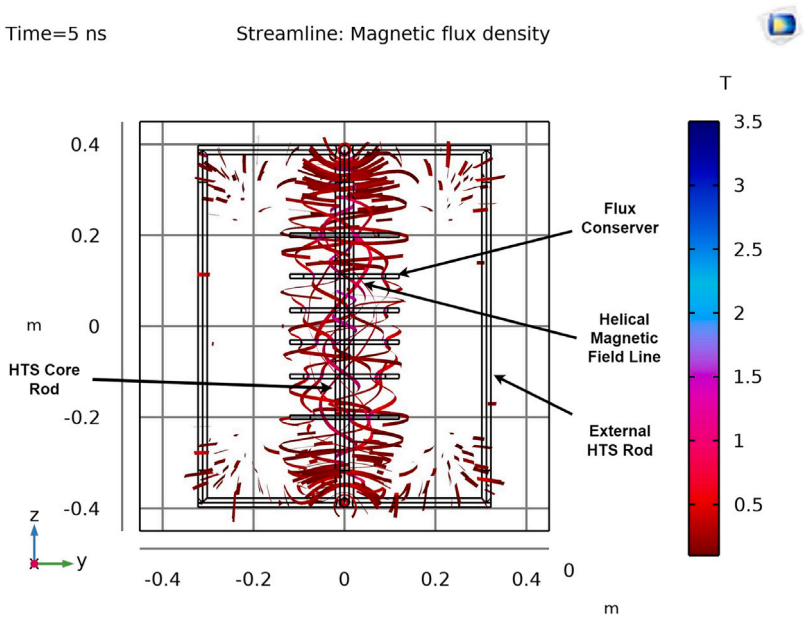

Fig. 4. Magnetic Field Lines Confined by Superconducting Flux Conservers. Six Yttrium Barium Copper Oxide (YBCO) superconducting rings confine a 500 Gauss axial magnetic field. A superconducting rod of the same material imposes an azimuthal magnetic field of 350 Gauss. Four parallel rods complete the electrical circuit. The time-domain transient analysis shows that the flux conservers successfully confine the total helical flux. (For interpretation of the references to color in this figure legend, the reader is referred to the web version of this article.)

present in [17] uses the parameters of the GE 90 series aircraft turbines. The Brayton cycle must operate continuously at a blade temperature of 1589 K for four years of transit and an unknown data-gathering period after the probe arrives at Pluto. [24] states that a GE 90 engine can survive 10,000 h before components require replacement, a little over a year at the maximum. This number includes the frequent maintenance aircraft engines receive aside from part replacement, something absent in a DFD servicing a spacecraft in deep space. Timelines in [11] show that a Brayton power conversion cycle has never flown to orbit. The design endeavor only begins in 2025, according to the latest timelines present in [11].

The Brayton cycle also necessitates massive radiators dependent on prototype composite material for mass reduction [25]. If the radiators use existing materials, the mass fraction of the radiators for a 9.5 MW DFD is 46% [20], and for the 1 MW reference DFD [11], the mass fraction is 22.7%. The entire power conversion system's mass fraction is 76% and 50%, respectively, including the radiators, the turbines, and the neutron shield cum heat exchanger. As stated in [17], the prototype composite is still underdeveloped, with no timelines provided. The authors cannot find further research on a radiator design using the prototype composite material or the material itself since [25] in 2014. Previous studies have dismissed other power conversion methods based on efficiency or technology readiness levels.

Finally, the results of previous work depend on empirical scaling relations and the specific powers of the subsystem components. Hence, the next logical step is to perform a detailed engineering design using first principles and simulation of the elements that support the reactor in generating thrust and electrical power. So far, research has focused on scientific rather than engineering feasibility for the DFD and the underlying FRC reactor. Furthermore, the body of research does not address the cost, manufacture, assembly, and testing required to certify the DFD for use in the industry. Therefore, the DFD design effort must now also concentrate on the engineering and financial aspects of the concept, such as weight, complexity, cost, and scalability, to realize the DFD's potential and promises.

3. Avenues for improvement

This section addresses the knowledge and technology gaps previously discussed in Section 2. This work proposes solutions to improve plasma confinement and reduce the design complexity based on the scientific literature. It also discusses the optimization of the engineering feasibility of the DFD concept with consideration of costs.

3.1. Introduction of azimuthal magnetic field

The authors propose the addition of a shielded superconducting rod to the FRC reactor's axis, which modifies the plasma's magnetization profile. The azimuthal magnetic field has implications for the plasma dynamics of the FRC reactor, which the authors very briefly cover in this work. This report focuses on the magnetohydrodynamic (MHD) power conversion system, which requires this modification.

The COMSOL Multiphysics 6.0 commercial code simulation shows that up to 70% of the axial field magnitude can be superimposed as an azimuthal magnetic field by the superconducting rod without compromising magnetic field line closure, a prerequisite for plasma confinement. Fig. 4 shows the nature of the magnetic field lines obtained from the simulation. Note that the axial magnetic field magnitude is 500 gauss for comparison with results published in [26], and all simulations ignore the magnetic field mirror effect. A simulation with a 3.38 T axial magnetic field shows similar results. The FC's design includes a safety factor to allow for excess current during operation, which allows for pinching of the axial magnetic field without changing the radius of the FC. The simulation files are available online with this work.

COMSOL Multiphysics was also used to model the effect of Flux Conserver (FC) spacing on the axial magnetic field confinement. The parameters calculated for a 1 MW DFD in later sections define the simulation geometry. The geometry models a superconducting HTS rod on the axis with several FCs. The spacing and number of the FCs are varied, and the simulation shows the flux ballooning in the results. The top and bottom faces of the geometry behave as perfect magnetic field conductors. The surface of the rod has a "Magnetic Field" boundary condition with an axial magnetic field value of 3.38 T. The azimuthal field magnitude equals 0.7 times the axial magnetic field magnitude. [11] recommends that the FC spacing is at max half the magnet radius, or equivalently the FRC chamber radius, to provide proper magnetic field confinement. Notably, this configuration leads to significant flux ballooning, as Fig. 5 shows. This work considers the

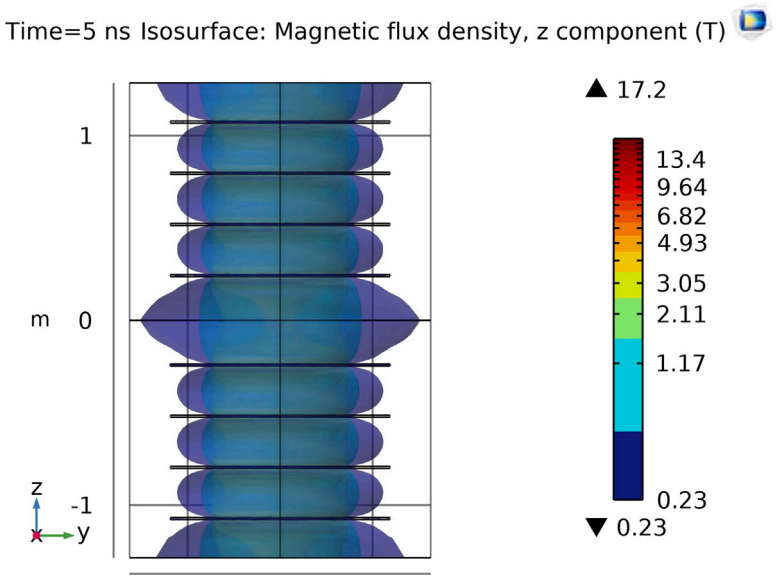

Fig. 5. Magnetic Flux Confinement Simulation with Large FC Spacing. This isosurface plot shows that the flux leaks out beyond the FCs in the middle. Note that the lowest magnitude isosurface has a magnitude of 0.23 T. The FC spacing is half the chamber radius, previously recommended in [11]. (For interpretation of the references to color in this figure legend, the reader is referred to the web version of this article.)

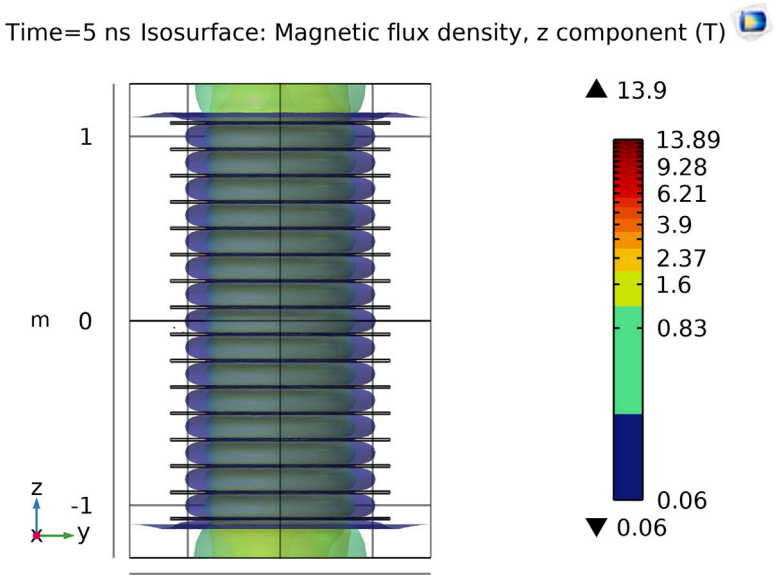

Fig. 6. Magnetic Flux Confinement Simulation with Optimal FC Spacing. This isosurface plot shows uniform flux confinement at all chamber points. Note that the lowest magnitude isosurface has a magnitude of 0.06 T. The FC spacing is a fifth of the chamber radius. (For interpretation of the references to color in this figure legend, the reader is referred to the web version of this article.)

maximum FC spacing as a fifth of the FRC chamber radius after several rounds of simulations. Any flux ballooning leads to plasma contact with the structural components and the RMF coils, damaging them. Fig. 6 shows the improved confinement due to the reduced FC spacing. The authors performed grid tests for all setups of both simulations and observed no significant mesh dependence of the solution on the grid.

The consequences of adding an azimuthal magnetic field to the plasma dynamics of the FRC reactor are numerous. Unfortunately, the authors do not have access to the proprietary software for simulating the FRC reactor's plasma dynamics. They hope that other workers in the field investigate this critical aspect of the device and our suggestion's impact. The authors briefly summarize some hypotheses based on published literature. The azimuthal magnetic field suppresses ion trajectory chaos observed in [3]. Chapter two of [27] provides precedent of an additional magnetic field used to control ion trajectory in a specific direction. This control mechanism affects D and 3He differently. Further work may explore if exploiting the mechanism to reduce D – D collisions in the FRC is feasible. Reducing the collision rate shall reduce the neutron fluence further to eliminate the neutron shield. [7] describes a fueling mechanism to reduce the amount of D present in the FRC at any given time. Hence, combining these techniques further reduces the neutron flux created by the fusion reactions in the FRC. The trade-off is the requirement of a very high D and 3He injector mass flow rate of 1×10^{15} per cm^3 per second for high-power reactors. High mass flow rate injection of ions is possible by modifying the Lithium Lorentz Force Accelerator (LiLFA), scaling its power consumption per ion to 20 eV, and operating current to 200 A [28].

Further, scientific literature suggests that the internal tilt mode growth rate exhibits non-ideal behavior if an azimuthal magnetic field is present, leading to better FRC stability [4]. The additional magnetic

field also ensures low-energy particles do not have magnetic flux null sites to pool in and leak out at high RMF magnitudes, a phenomenon observed in simulations [29].

Additionally, exploiting the azimuthal magnetic field to create an electron density imbalance near the outer surface of the FRC shall improve RF penetration and reduce the subsystem power requirements. The proposal is feasible due to the magnetic field's strong magnetization of electrons along the azimuthal field lines. Using the equations provided in [30] and the peak magnetic field norm value of 60.4 T near the surface of the HTS Core Rod surface in the COMSOL simulations, the Larmor radius of a 120 KeV electron near the rod is 1.365×10^{-3} cm, and the radius for a 120 KeV 3He ion is 5.066×10^{-2} cm. Thus, the magnetic field preferentially restricts electron motion by one order of magnitude relative to ion motion. The magnetic field suppresses electron diffusion [27] in the radial direction. COMSOL simulations presented later show an induced electric potential difference of the order of a kilovolt between the rod's surface and the chamber's inner surface because of the SOL plasma flow. The design presented in the next section uses anodized metal for construction which prevents electrical shorting of the surfaces and provides evidence supporting the formation of the expected plasma structure. The electrons must be thermally ejected from the rod to sustain this configuration, as the generated electric field causes the ions to diffuse into the electron-rich region. This hypothesis can be verified and tested by workers with access to Particle-In-Cell (PIC) simulation codes, Molecular Dynamics coupled Monte Carlo simulation codes [31], and single-particle Hamiltonian simulation codes and the means to run them.

3.2. High power radio-frequency systems

Practical FRC reactors require high-power radio-frequency (RF) systems. Currently, only inductive output tubes (IOTs) satisfy the project's power, frequency, and footprint specifications [32,33]. Commercial units with an average output power of 100 kW and efficiencies greater than 65% are available [34]. Experimental results presented in [33] show efficiencies as high as 89% in D – class operation under laboratory conditions. The caveat of deploying IOT technology is the requirement of solid-state high-power RF generators for the IOT amplifier input [35]. [11] presents findings that resolve this issue. Another concern is power transmission and the associated losses. Some groups have attempted to address the inductance of the RF transmission lines and have shown success. Accurate modeling of the interaction of the plasma with the RF generator and transmission lines has informed designs that improve efficiency during operation [36]. Currently, the underlying FRC reactor has not seen such investigations. Thus, characterizing conventional conductors' RF properties at liquid helium temperatures is necessary for efficient power recirculation.

3.3. Direct fusion drive — power conversion architecture

Three subsystems, namely the power generation cycle, cryostat system, and thrust generation mechanism, can be optimized from the previous architecture. The radiator system and the Brayton power generation cycle are a source of complexity in the DFD's design. Furthermore, a prototype carbon composite material, which is currently undergoing development, must be used to fabricate the radiator if large radiator masses are unacceptable [9]. The authors propose a Magnetohydrodynamic (MHD) generator to replace the current power generation cycle. [11] has considered this possibility but dismissed it on the grounds of excess superconductor requirements and the use of refractory electrodes. The following discussion shows that an MHD generator performs better than the current Brayton cycle system in terms of efficiency and mass fraction while being studied in the literature as thoroughly as the Brayton cycle.

Theoretically, there are numerous studies on MHD generators, with literature dating back to the 1970s [37]. Technology has advanced to the point that experimental work has increasingly become relevant. The efficiencies of lab prototypes do not approach a conventional power generation cycle [38,39]; however, the lab prototypes have never investigated efficiencies if the working fluid is fully ionized. Theoretically, the literature indicates equivalent or improved efficiencies if fully ionized and magnetized plasma is used [37,39–42], which is the case here. A conceptual MHD generator from [43] is shown here in Fig. 7.

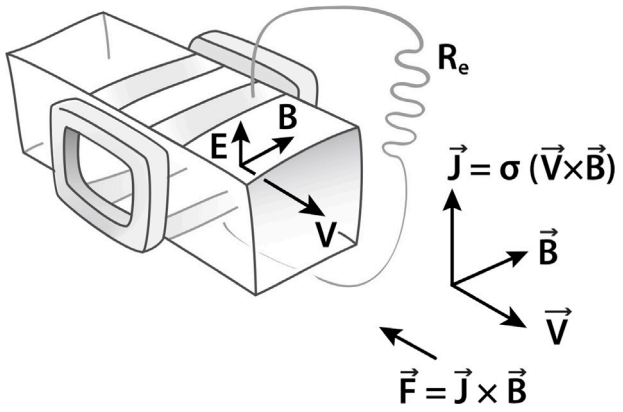

Fig. 7. Basic Principles of Magnetohydrodynamic (MHD) Power Generation. The top left shows a simple geometry to generate an electrical current using plasma flow and a magnetic field. The middle right shows the vectors of the electromagnetic forces and currents within the geometry. Finally, the force vector on the bottom illustrates the plasma kinetic energy conversion into the device's current output via flow deceleration. *Source:* Reproduced without modification from [43] under the CC-BY-SA 4.0 License.

An MHD generator has no moving parts, requires minimal maintenance, and can operate continuously at the time scales relevant for deep-space missions. It does not require a radiator or prototype advanced materials and has the unique advantage of generating minimal waste heat. Any energy not extracted from the plasma flow to produce electrical current produces thrust, barring any isentropic losses. The current Brayton power cycle exhausts 17 to 27% of the fusion power as waste heat which can be recovered as usable electricity if an MHD generator is used [1,7,8,10,12,19,20,44,45]. Finally, the DFD has lower heat fluxes than large tokamaks like the ITER, and conductive plasma-facing materials such as tungsten and diamond composites have already been developed in the literature to withstand the much harsher conditions present in those devices [46,47]. These materials are candidates for the MHD generator electrodes in future detailed investigations, having already seen much testing and evaluation [48–50].

The authors set up preliminary resistive MHD simulations in COMSOL Multiphysics to explore the application of an MHD generator to the DFD. The 2D axisymmetric simulation made the following assumptions to balance the fidelity and solution time. The simulation was time-independent and did not capture any plasma instabilities. Additionally, it assumed a fully magnetized and thermalized plasma at the inlet. Multiple simulation results showed an absence of azimuthal plasma current. The simulations also showed a non-physical shock at the device's exit if the flow had axial electrical conductivity. The shock formation was due to the boundary condition of a supersonic flow at the exit. Since the device's outlet serves as the nozzle's throat, the simulation must enforce this condition such that the nozzle can expand the plasma for thrust downstream. Hence, the model only considered the radial electrical conductivity calculated from the Spitzer Resistivity using equations provided in [30] at the inlet, assuming no variation in space. The authors assumed no variation of electrical conductivity in space because the plasma temperature did not vary significantly as the plasma decelerated in the device.

The simplifications resulted in an MHD generator model with a supersonic inlet and exit with a converging taper of 0.1 degrees added to improve solver stability. The taper ensured that the nonlinear solver

Table 1
MHD generator outputs for 1 MW DFD with 3.38 T axial magnetic field.

Azimuthal magnetic field (T)	Outflow power (kW)	Load power (kW)	Electrode voltage (V)
1.24	952.82	47.16	1504.9
1.68	916.32	83.68	2004.1
2.16	870.09	129.97	2496.1

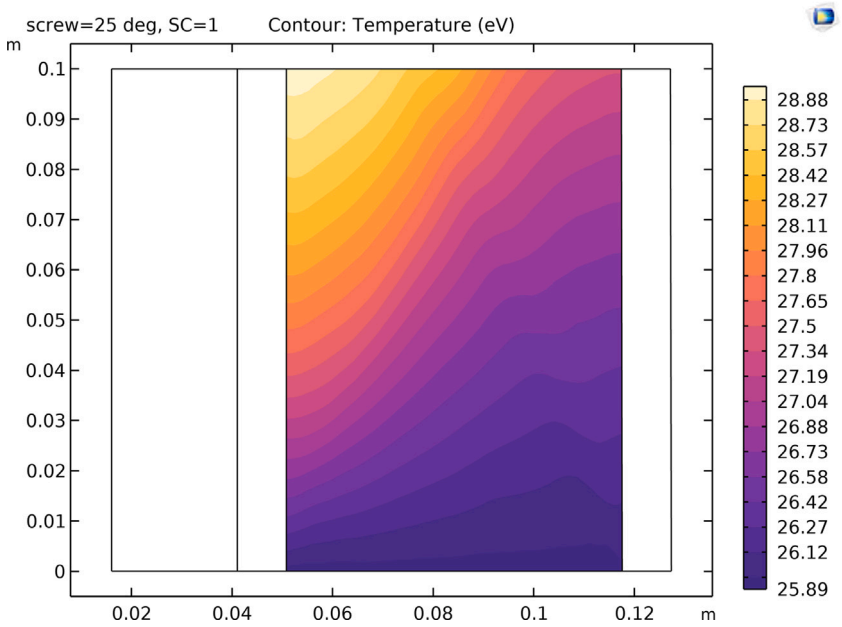

Fig. 8. Temperature Contours of Plasma Inside an MHD Generator. The solution is for the case of a 2.16 T azimuthal magnetic field. The plot shows that the temperature variation is around 10% over the MHD generator, validating the assumption of constant plasma conductivity. The two boxes beside the contour represent the electrodes in contact with the plasma. The inner electrode is grounded. The leftmost box represents a thermal and electrical insulator with the magnetic field boundary condition assigned to its leftmost edge. (For interpretation of the references to color in this figure legend, the reader is referred to the web version of this article.)

converged to a physical solution that described an MHD generator instead of an MHD pump. The inlet flow power of the device was set equal to the FRC reactor power, and the simulation used hydrogen plasma for the working fluid. The model computed the input fluid variables, such as plasma temperature and pressure, using the total inlet enthalpy, mass flow rate and Mach number as parameters. For a 1 MW reference DFD, a mass flow rate of 80 mg/s and a Mach number of 3 resulted in inlet temperatures and number densities in agreement with values published in [11]. The simulation stepped the azimuthal magnetic field magnitude as a fraction of the axial magnetic field magnitude. For each azimuthal magnetic field strength, the solver gradually increased the plasma conductivity to the physical value, equivalent to initially suppressing induced plasma currents and simulating a fully magnetized input plasma. The MHD generator electrical output had a resistance of 50 ohms, which the simulation lumped into the resistance of the outer electrode.

In this work, the outlet enthalpy and solution grid dependence provided the means to verify the solution. The authors found no grid dependence of the solution and excellent agreement of values between simulations which refined the mesh by 12% from 621 elements. The sum of the outlet power with power dissipation in the plasma and load agreed with the inlet power to within 0.1%, further certifying the sanity of the solutions. The authors found this verification level satisfactory for the preliminary evaluation stage of the concept. Table 1 shows the simulation results for a 1 MW DFD with an axial magnetic field magnitude of 3.38 T and an MHD generator length of 10 cm. Fig. 8 shows the flow temperature contours for the maximum load power configuration.

The COMSOL simulations demonstrate that an MHD generator can extract a significant fraction of the flow enthalpy for a plasma with characteristics similar to DFD exhaust. Further, the MHD generator's dimensions are compact and produce enough power to be competitive with a Brayton cycle-based system. The device also does not breach the azimuthal magnetic field magnitude limit stated earlier in this article within the plasma domain. The simulations also show that in the case of the 50 kW DFD presented later, an identical device with an azimuthal magnetic field magnitude of 2.77 T can extract over 22.1% of the input flow power, which makes a DFD with a Q factor of 5 feasible. Based on the above results, the authors consider detailed MHD generator design and simulation worthy of a separate investigation in future articles.

3.4. Direct fusion drive — cryostat architecture

Next, consider the current cryostat system. Aside from the neutron shield, superconductor mass is the deciding factor for the overall reactor weight [9]. Recently, second-generation high-temperature superconductors have proven their engineering limits by operating in background magnetic fields of over 12 T and generating 19 T of axial magnetic field [51]. The feat is possible due to improvements in commercial Rare Earth Barium Copper Oxide (REBCO) superconducting material and the application of high-temperature superconductors at traditionally low temperatures. Using REBCO commercial superconducting tape at liquid helium temperature significantly reduces the physical dimensions of the DFD in our work because the critical tape current increases to 1.5 kA from 160 A at liquid nitrogen temperature [52].

More recently, commercial High-Temperature Superconductor (HTS) tape has achieved a capacity to carry 1.1 kA at liquid helium temperature with a thickness of only 43 μm [23]. Additionally, HTS tape exhibits stable electrical characteristics for a wide temperature

margin at liquid helium temperature resulting in more fault-tolerant and quenching resistant designs [53]. Bruker HTS tape shows only a 25% decrease in critical current as the temperature varies from 4.2 K to 10 K inside a parallel magnetic field of 3 T [52]. A safety factor during the design of the superconducting solenoid can easily account for this variation. This resistance to changes in HTS properties damps the effect of changes to the critical temperature of the superconducting material due to neutron radiation damage on DFD operation [22]. After completing design calculations in this work, ideally, HTS tape of carrying capacity greater than 800 A at liquid helium temperature with sub-15-micron thickness is required for practical reactors to ensure reasonable radial dimension and mass of the superconducting solenoids in the flux conservers. As noted in the previous section, no other superconductor class can satisfy these requirements.

Interestingly, the HTS industry has no sustained demand for its product, affecting its viability [53]. A collaboration between HTS tape manufacturers and investigators working on the DFD to tailor a product variant for use in the underlying FRC reactor may ensure that both parties needs are satisfied. For instance, the authors suggest a tape design, drawing from the results of the design exercise, using High Modulus Carbon Fiber (HMCF) electroplated with Nickel and Copper instead of the proprietary Hastelloy currently used as the substrate. A series of steps, namely, the initial treatment of the HMCF with a Nitric Acid bath and subsequent electroplating with Nickel and Copper, can be performed continuously to create a strip that acts as a substrate [54]. Afterward, pulling the strip through a dye constrains the dimensions of the strip and improves the surface finish. The resulting substrate possesses a yield strength greater than 2000 MPa and 32% lower density than Hastelloy alone, along with comparable electrical conductivity to bulk Copper [55]. These properties significantly reduce the cost and weight of the HTS tape. The improvement in substrate strength, which is at least double that of most HTS tape substrates [53], also helps achieve the sub-15-micron target.

Thus, the authors recommend conducting a detailed investigation into operation at liquid helium temperature based on the design presented in the following section to exploit the above advantages. Maintaining the necessary low temperatures in the vacuum of space is more straightforward, as conductive and convective heat transfer is absent. The remaining radiative heat transfer problem has already been addressed in [56] using thin aluminum foils of low blackbody emissivity to reflect incoming radiation. The Spitzer space telescope [57] and the AKARI space telescope [58] operations show that achieving liquid helium temperatures is possible for extended periods [59]. Passive cooling using a multi-layer insulation sunshade is adequate to achieve temperatures of 20–30 K. The temperatures reduce further as the space vehicle moves away from the Earth, a source of infrared radiation. In particular, the Spitzer space telescope's vapor-cooled design is relevant for further optimizing the cryostat design proposed in this work [57]. However, none of these space telescopes has an internal heat source like the DFD, illustrating the challenges ahead.

3.5. Direct fusion drive — thrust generation architecture

Until recently, scientific literature has only utilized deuterium as the reaction mass without providing detailed reasoning. Deuterium is exorbitantly costly at $ 13,400 per kilogram [60], and the proposed crewed Mars mission is estimated to utilize around 157.65 tons of deuterium as the reaction mass [10]. Such a mission would require a propellant tank comparable to the space shuttle's external liquid hydrogen tank [61]. Tank dimensions aside, even exploratory missions that do not require similarly large quantities of deuterium struggle to justify the steep cost of fuel which serves no other purpose than to produce thrust by being ejected out of the spacecraft. The DFD design has switched to hydrogen gas reaction mass without providing further reasoning [20].

The SOL flow is an integral feature of the PFRC. However, the observed disruption of the SOL flow caused by the heated FRC blow-off in the PFRC – 2 is brought up in [11] but not addressed in any following publications. Instead of adding reaction mass to the SOL, this work proposes a system that uses downstream high-energy fusion products to heat and ionize a working fluid while providing several benefits. This section also examines the propellant selection process in greater detail than before. Such a system enables the reaction mass to be hydrogen gas without affecting any other DFD subsystem, doubling the engine's specific impulse while reducing propellant cost by a factor of 3,000 [62]. It also allows the usage of molecular propellants like water, methane, and ammonia as the reaction mass, which is desirable if the propellant infrastructure's cost, size, and weight constraints are extreme, albeit at significantly lower specific impulse [63,64]. This configuration also allows neutral beam fuel injection methods without fear of disturbance by the reaction mass's flow in the SOL around the FRC. In addition, designing a single plasma processor presents significant advantages. The component can inject the reaction mass and extract electrical current from the plasma flow. [38,39,42], and the results of the preliminary simulations presented here show that such a device is feasible. The authors intend to study, simulate and verify these claims in greater detail in future publications. The new thrust generation mechanism implies that the design for this component is complex, and detailed simulations, beyond the results presented here, must prove the feasibility of the concept with the above reaction mass choices. However, it potentially opens the door for the DFD to operate in atmospheric, suborbital, orbital, and deep-space environments while ensuring the operational costs remain feasible. The reduced cost and the added flexibility of the overall design shall accelerate the industry's and society's adoption of the DFD [65].

4. Engine design methodology

This section presents the methodology used to design a DFD and the underlying FRC reactor, incorporating the previous section's proposed changes. It provides data on the engineering relations which constrain the engine's dimensions and detail material selection and compatibility. This section also discusses the expected requirements for a future prototype design and a full-scale DFD. Instead of using relations used in previous design efforts [11,17], this work uses the equations presented from ion heating and particle trajectories simulations in papers by Cohen et al. [3,29]

4.1. Field reversed configuration reactor

Aside from focusing on engineering feasibility, this work stresses the scalability of the resulting design. One of the reasons fossil fuel-based energy sources are ubiquitous is the scalability of the concept of the internal combustion engine and the gas turbine, with both possessing high specific power [65]. The FRC reactor and the DFD must match that scalability and flexibility to achieve widespread adoption. As a result, this section uses a 50 kW fusion power DFD with a Q value of 5 to demonstrate the design methodology. The Q value is the ratio of the fusion power to the input RF power. Hence, the RF system power is 10 kW, achievable by a relatively inexpensive solid-state system built in-house [66] or purchased from a commercial vendor [67]. This design exercise selects a 50 kW fusion power target to ensure a cost-efficient design. If the fusion power target drops further, the reaction mass does not have enough power input to produce a fully ionized plasma at the flow rates (> 50 mg/s) expected in an actual DFD [2]. This section also presents calculations for a 1 MW DFD and compares the results with the 1 MW reference design in [11]. The main aim is to uncover issues in the assembly method and fundamental engineering hurdles in building a DFD. The design effort does not explicitly optimize the weight or cost; a future prototype's design process should focus on that exercise. This endeavor aims to design a working DFD that requires minimal

Table 2
Key calculated parameters for the 50 kW prototype and 1 MW prototype.

Calculated parameter	50 kW DFD	1 MW DFD
Fusion Power (P_{fus})	0.05 MW	1 MW [11]
Q Value	5	5
Ion Temperature (T_{ion})	120 KeV [11]	120 KeV [11]
Aspect Ratio (K_{ref}) [6]	5	5
HTS Critical Current @ (4.2 K, 3.5 T) [23]	1150 A	1150 A
HTS Operating Current @ (4.2 K, 3.5 T)	920 A	920 A
Fusion Product Confinement Factor (B_{zCtrl})	1	2
Azimuthal to Axial Magnetic Field Ratio	0.7	0.7
RMF to Axial Magnetic Field Ratio ($B_{rmf\,Ratio}$) [6]	0.0037	0.0037
MLI Insulation Thickness (t_{ins})	2.5 cm	2.5 cm
Axial Magnetic Field (B_z)	29939.7 Gauss	33842.5 Gauss
Titanium R50550 Plate Thickness (t_{plate})	0.479 cm	0.977 cm
Separatrix Radius (R_s)	11.05 cm	30 cm
Chamber Radius (R_{chm})	29.33 cm	46.75 cm
HTS Solenoid Outer Radius (R_{HTS})	40.95 cm	65.33 cm
DFD Radius	49.79 cm	78.15 cm
DFD Length	146.63 cm	233.76 cm
Empty Cryostat Volume	0.594 m^3	2.511 m^3
Liquid Helium Mass	74.25 kg	313.875 kg
Number of Flux Conservers in Prototype (N_c)	32	36

capital and labor hours for manufacture, which leaves time to overcome engineering hurdles and address concerns that emerge throughout the design process. Further, the 50 kW design does not produce any measurable thrust due to its low fusion power target. Hence, the only focus of this work is on system verification and integration within that design.

The dimensions of the FRC reactor and its supporting components, such as the injectors, are calculated from various scientific scaling relations in the scientific literature [3,29]. The RF subsystem's components are the only ones to use an empirical specific power scaling for their design. Table 2 shows key parameters calculated for constraining and dimensioning the CAD components and their notations in equations provided in the text. A complete list of all parameters and equations used for the calculations and the CAD file are available as supplementary data.

Firstly, the reactor radius and axial magnetic field magnitude are determined using mathematical scaling equations in [3,29]. [3] also states that the fusion power for the FRC reactor is proportional to the chamber volume leading to Eq. (1), used to calculate the separatrix radius. Then, the algorithm uses Eq. (2) using the results of [29] to calculate the axial magnetic field magnitude with the B_{zCtrl} variable, which controls the fusion product gyroradius by augmenting the axial magnetic field magnitude. The equations do not reference plasma parameters such as plasma density or the plasma beta as they are held constant at the values provided for the RFRC during scaling and cancel out.

$$R_s = 30 * P_{fus} * \left[\frac{5}{K_{ref}}\right]^{\frac{1}{3}} \tag{1}$$

$$B_z = 20000 * B_{zCtrl} * \left[\left[\frac{T_{ion}}{6}\right] * \left[\frac{10}{R_s}\right]^2 * \left[\frac{50}{\pi * K_{ref}}\right]^{0.5} * \left[\frac{0.001}{B_{rmf\,Ratio}}\right]^{1.5}\right]^{\frac{1}{3.5}} \tag{2}$$

Once the magnetic field magnitudes are known, the chamber radius is the HTS superconducting rod's radius added to the separatrix radius and the ion gyroradius. Then the method discussed in Section 2 provides the radial thickness of the HTS pancakes. Finally, the algorithm finds the total radius of the DFD and its length. The supplementary data provides the equations used in the algorithm, and Fusion 360 calculates them sequentially to constrain the dimensions of the various components in the CAD.

The properties of SuperPower's SCS4030-AP REBCO HTS tape used in this design are available in [23]. A prototype design that selects the axial field magnitude to be around 3 T is most efficient in mass, as it enables the use of the total carrying capacity of the HTS tape. While increasing the field magnitude may reduce the chamber dimensions by improving confinement, the corresponding solenoid radial thickness increases cancel any overall gains. The topmost and the bottommost flux conservers create the magnetic mirror effect required to hold the FRC in place by operating at a higher current by reducing the safety factor. Further, due to the cost of the HTS tape and its weight, a design must aim to reduce the amount used in construction. In collaboration with the industry, further improvements to the HTS tape enable lighter and more compact FRC reactors, as discussed in section 3.4 with an example.

4.2. Superconducting systems and cryostat

[56,68] detail the insulator thickness and radiative heat transfer considerations for a cryostat. While the DFD possesses cylindrical symmetry, the authors constructed the cryostat as an octagonal shell. While not relevant for this scale, the dimensions quickly become untenable as the specifications move toward a practical FRC reactor and DFD. An octagonal body is not an efficient pressure vessel due to stress concentration regions at the vertices, similar to the observations in [69]. However, its construction is straightforward, requiring only plates, a pre-processing machine to cut them to size, and welding. The simple construction method facilitates manufacturing in Earth orbit or the Moon with general-purpose tools and machinery. In contrast, a cylinder requires specialized sheet metal shaping machines for thick sheets and large bend radii.

In addition, [11] and all other studies [1,7,8,10,12,19,20,44,45] assume that the spacecraft is launched into Low Earth Orbit (LEO) to begin its mission. However, no previous research has included the effect of launch loads on the DFD's structural integrity. The authors performed a structural load simulation in Fusion 360 for 6 Gs of axial loading based on the SpaceX Falcon Payload User's Guide [70]. Due to its numerous components, a point mass substitutes the FRC structure. Another point mass substitutes for the internal FCs in the plasma processor. The bottom face of the nozzle wall fixes the simplified

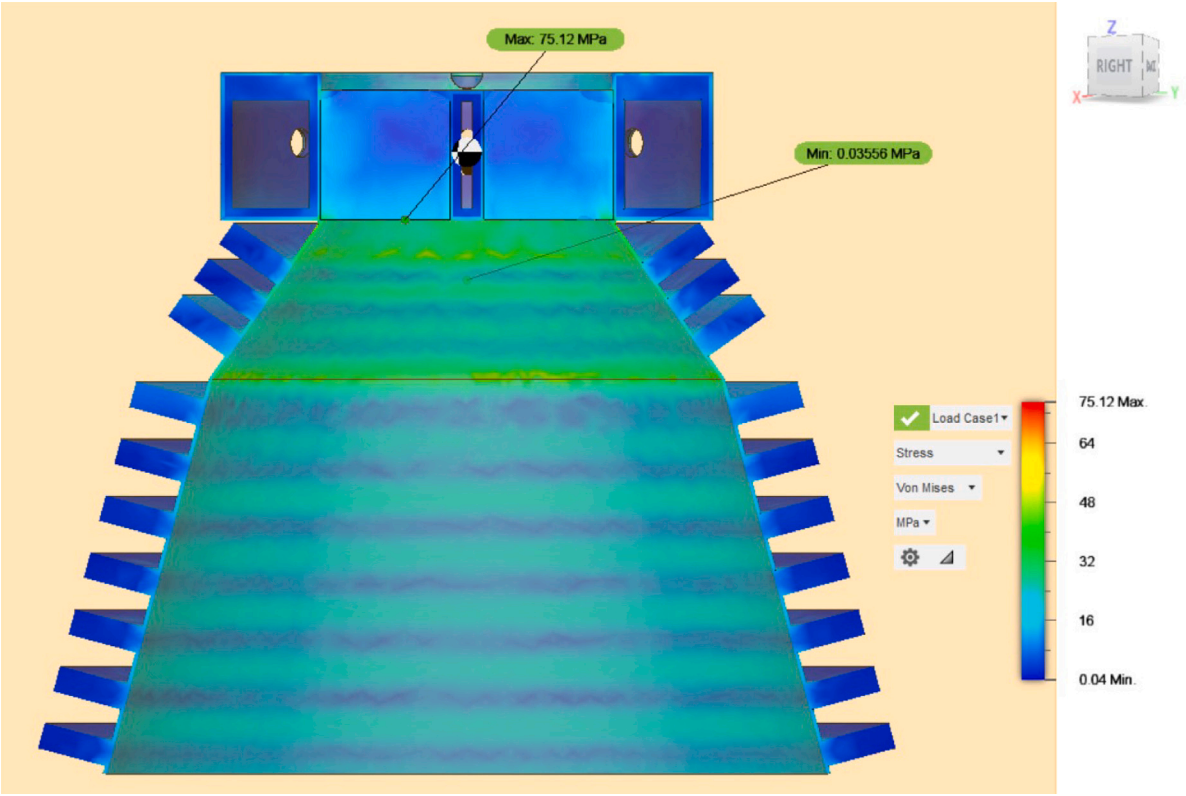

Fig. 9. Structural Analysis of a Simplified 1 MW DFD Under 6 G Axial Load. The yellow plane slices the geometry to show the internal stress contours. The FRC reactor and plasma processor FCs are accounted for as a point mass, shown as the black and white circle. The maximum stress occurs around the transition region in the nozzle inlet. (For interpretation of the references to color in this figure legend, the reader is referred to the web version of this article.)

geometry for constraining the analysis. The results show a minimum safety factor of 1.45 and a maximum stress value of 75.12 MPa, lower than the allowable stress value, on the inner side of the nozzle inlet. Fig. 9 illustrates the results of the analysis. Thus, the structural components comply with international rocket engine combustion chamber and pressure vessel design standards.

Concerning the design standards, the cryostat and the FRC reactor core design conform to the American Society of Mechanical Engineers (ASME) Boiler and Pressure Vessel Code (BPVC). It uses commercial titanium alloy R50550 plates coated with 0.005 mils Tantalum foil to reduce plasma sputtering [26] and commercial aluminum alloy A95083-O parts for nonstructural members. The selected alloy conforms to the ASTM SB-862 standard [71]. The Cryogenic Materials Data Handbook rates R50550, listed as "Commercially Pure Titanium", for service at liquid helium temperatures. Its yield strength (70 ksi grade, annealed variant) is 68 ksi at room temperature and improves to 172 ksi at service temperature [72]. The algorithm uses Eq. (3) to find the plasma pressure (P_{plasma}) in units of MPa from [30]. This work uses magnetic pressure to design the pressure vessel because it represents the maximum load on the structure. Previous publications [11] show that introducing plasma into the FRC reduces the overall magnetic field magnitude. However, the pressure vessel design must consider the situation of the DFD during startup, where the maximum axial magnetic field magnitude is present without the easing effects of the induced plasma currents. The algorithm then utilizes Eq. (4) with the Allowable Stress (S_a) set to 109 MPa from the BPVC Allowable Stress Tables and an additional safety factor of 1.25 to calculate the required plate thickness (t_{plate}).

$$P_{plasma} = 3.93 * 0.101325 * \left[\frac{B_z}{10000}\right]^2 \tag{3}$$

$$t_{plate} = \frac{P_{plasma} * R_{chm}}{S_a * \left[\frac{2.529}{1.25}\right] - 0.5 * P_{plasma}} \tag{4}$$

The authors propose using Metal Inert Gas (MIG) welding with commercial titanium alloy ERTi-12 as the weld filler material during fabrication. The non-welded seams, some of which are load-bearing, are soldered using standard SAC305 lead-free solder for relatively high strength at cryogenic temperatures [73], easy maintenance, and disassembly with minimal tooling. Alternative joining materials include epoxy resin systems and thermoplastics [74]. Studies have evaluated the Tungsten Inert Gas (TIG) welding method, similar to the MIG welding method, in a low gravity environment and shown that welding is possible. Only weld qualities such as the grain size and cooling rate changed from controls welded at Earth gravity, implying a more ductile join with augmented grain sizes [75]. Studies have considered soldering in low gravity environments and indicated that it is possible but with a 32% penalty in joint strength. The strength penalty is mainly due to the retention of flux-induced porosity because the buoyancy-induced expulsion of the vaporized flux is absent [76]. Future work must select a different temporary joining method or address the issue of solder joint porosity.

The authors also considered additive manufacturing (AM) of the DFD's components. AM is relevant in two scenarios. In Space AM (ISAM) can enable orbital DFD manufacturing, requiring only the raw materials and remote infrastructure to be launched [77]. However, [78] shows that ISAM technology is nascent and has not seen any experimental validation for metal printing. Further, the physics affecting the material deposition is not fully understood even though previous investigations [79] provide some missing data. AM on Earth is more relevant for aerospace components. [80] discusses titanium alloy brackets and their structural characteristics manufactured for the Juno probe using

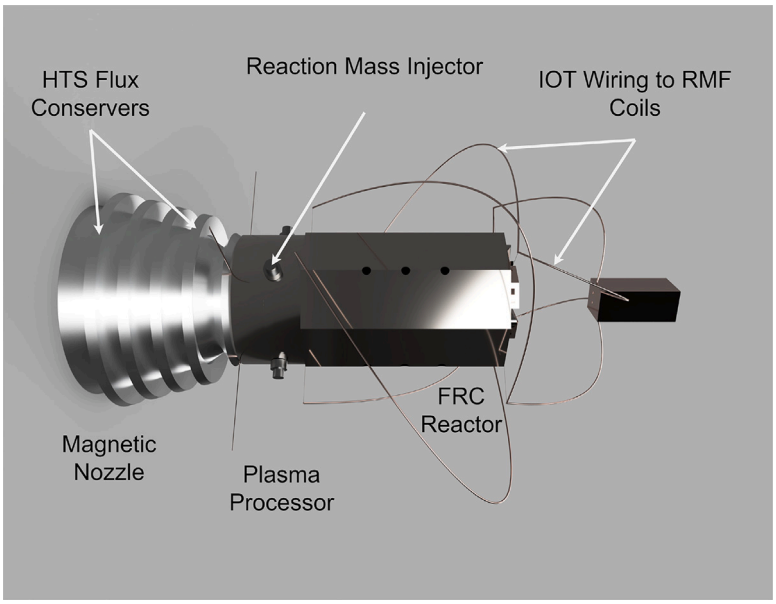

Fig. 10. A Rendering of the side view of the assembled 50 kW DFD.

AM and traditional machining. At this time, the design in this paper does not utilize any AM to manufacture DFD parts due to the untested nature of the technology for metallic components and the relatively simple geometry. However, AM technologies have shown success with titanium alloys which led the authors to incorporate titanium alloy R50550 into the design, making it amenable to AM should the need arise.

4.3. Fuel injection and radio-frequency heating systems

The ion injectors occupy the gaps between the HTS Core sections that act as a "cap" on the top of the DFD. Two cathodes separated by a pair of copper plates injects 3He ions and D ions, with the 3He ions injected near the HTS Core rod, in each injector. The HTS Core rod sections require a Tungsten coating over an additional hard-anodized titania electrical insulation layer [81] using Chemical Vapour Deposition (CVD) to ensure the rod surface absorbs the incoming X-ray radiation. The absorbed radiation leads to an increase in film temperature [21,82]. The absorbed radiation reduces the film's heating requirements during operation and reduces radiation losses by recycling the energy. The mathematical scaling relations for the injectors are present in [28,83]. The injectors are scaled based on 200 A of total ion input for each species, with the HTS Core pipe surface ejecting 400 A in thermal electrons to maintain global charge neutrality. The authors selected the current magnitude based on the density estimate of 1×10^{14} per cm^3 for a practical reactor [3]. The Lithium Lorentz Force Accelerator (LiLFA), the basis of these dummy injectors, has a record of operation up to 7 kA, which provides ample margin for future reactors [83]. All injectors are solid copper black boxes in this study, which only illustrate the approximate size and weight of the devices fitted into a physical DFD.

Next, the authors focus on the Rotating Magnetic Field (RMF) plasma heating system. The design of the RMF coils utilizes data published in [13]. The RMF coils use a standard Oxygen-Free High Thermal Conductivity (OFHC) copper plate of 0.15 cm thickness. A wire electrical discharge machine (EDM) machines a metal plate into a spiral according to the dimensions, calculated analytically using [84], required to achieve the necessary magnetic field magnitude. The design assumes 35 A of coil current, with the cryostat as ground and the ambient temperature as 50 K [85]. The design uses the liquid helium boil-off and reduced insulation thickness to ensure that the chamber walls maintain their temperature in this prototype. The decision also enables the RMF coils to operate at temperatures where the calculated dimensions reasonably fit inside the FRC chamber along the surface. Future prototypes may include reaction mass pipes to preheat the hydrogen gas before injection into the plasma processor while cooling the FRC chamber.

4.4. Mass analysis of designed prototypes

Fig. 10 illustrates the assembled DFD with the underlying FRC reactor, the RF sources and wiring, the liquid helium cryostat, the plasma processor, and the magnetic nozzle. Figs. 11 and 12 show the internals of the 50 kW DFD in greater detail and from a different viewpoint.

Table 3 details the mass breakdown of each subsystem in the prototype. Fusion 360 produces the mass values for each solid in the CAD using its material and volume. Thus, by calculating the dimensions of a solid using the scaling relations and assigning an appropriate material, the authors tally the mass of each component or subassembly. A component's structural mass includes all bodies, including the winding supports for the HTS tape in each FC and the insulation materials. Table 3 also shows available data reproduced from [11] for the 1 MW reference design of the DFD. The cells containing "NA" indicate that no data is available.

Each flux conserver consists of a titanium casing made of R50550, within which a double pancake of tape exists. The magnetic field magnitudes determine the radial thickness of the solenoidal pancakes. The design aims for minimal flux leak and chooses the axial spacing inferred from the previous section's simulations.

Eq. (5) provides the HTS superconductor mass required for the FRC's FCs, assuming a maximum uniform density of 8.89 rounded up to 9 g per cm^3 of Hastelloy C-276 [86] as the density of the specific Hastelloy alloy used for its substrate is unknown [23].

$$m_{HTS} = N_c * \pi * \left({R_{HTS}}^2 - \left(R_{chm} + 2 * t_{plate} + t_{ins} \right)^2 \right) * 0.8 * (9 - 4.5) * 0.001 + 4 * m_{HTSCore} \quad (5)$$

Eq. (5) assumes that each flux conserver has constant inner and outer radii and a height of 0.8 cm, which is twice that of the tape width of SuperPower's SCS4030-AP REBCO HTS tape, which comprises the

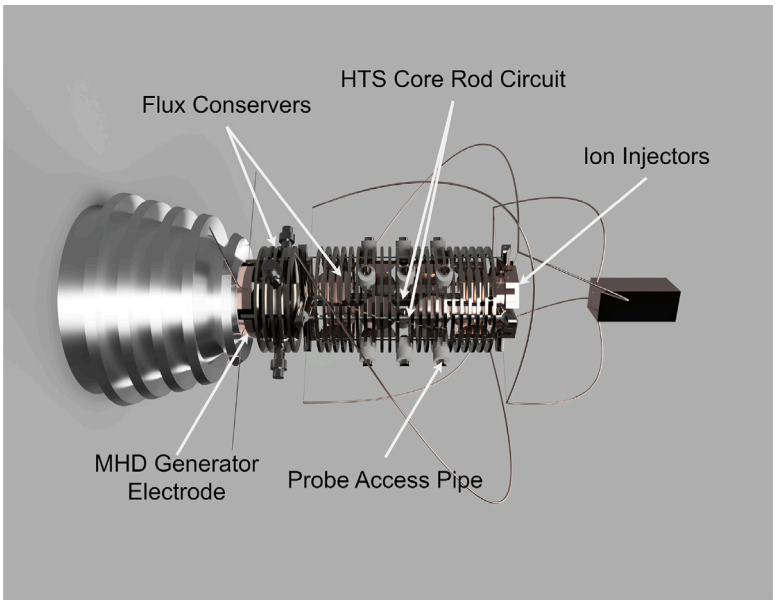

Fig. 11. A Rendering of the Assembled 50 kW DFD side view without Structural and Thermal Insulation Components. The RMF coils are visible through the set of FCs of the FRC reactor.

Table 3
Prototype mass breakdown and subsystem mass fractions.

Subsystem	50 kW DFD (kg)	1 MW DFD (kg)	1 MW Reference DFD (kg)
FRC FC Structural Mass	26.4	57.6	NA
FRC Structural Mass	698.7	3432	122
HTS Core Rod Mass ($m_{HTSCore}$)	18.8	33	NA
FRC RMF System Mass	421.2	7759	118
FRC Injector System Mass	137.5	439.1	NA
Total FRC Reactor Mass	1815	11663	NA
Median Plasma Processor FC Structural Mass	18.3	90.5	NA
Total Plasma Processor Mass	629.9	1354	NA
Magnetic Nozzle Mass	585.9	3258	NA
Total Design Mass	3030	16275	1345
Additional FRC HTS Tape Mass (m_{HTS})	292.9	802	NA
Total Prototype Mass	3322.9	17077	1345
Mass Fraction of Subsystems in FRC Reactor			
RMF System	23.207%	66.527%	8.8%
Injector System	7.576%	3.765%	NA
Mass Fraction of Subsystems in Prototype			
HTS Superconducting System	9.380%	4.696%	NA
Power Generation System	18.956%	7.929%	38.1%
Thrust Generation System	17.632%	19.078%	NA

double pancake. Since the flux conservers in the CAD are solid titanium bodies, the equation subtracts the density of the R50550 alloy, which is 4.5 g per cm^3, from the assumed material density. Then the HTS mass equation multiplies the value by the number of flux conservers in the prototype and adds four times the mass of the HTS Core rod to account for the unmodeled HTS tape required to complete the electrical circuit.

As noted earlier, the plasma processor requires intense development to fulfill its specifications. Hence, its design and weight here are conceptual. As the magnetic nozzle depends on the plasma processor's output, its dimensions and weight are also conceptual. Also, note that the additional HTS tape mass lumped in for the nozzle FCs is an approximation providing best-case values that ignore the larger radii of this component relative to the FRC. However, the CAD uses parametric paradigms to update the model components as input variables change. In Table 3, the authors observe that the pressure vessel is over-engineered, accounting for about 38% of the mass of the 50 kW prototype. Since a vacuum environment, such as outer space, minimizes heat leak into the cryostat, a conduction cum vapor-cooled cryostat design offers significant savings in weight and material cost [87]. Ideally, a practical FRC reactor must maximize the cumulative mass fraction of the RMF and Injector Subsystems, roughly achieving equal masses for them both. The design of future prototypes must account for these observations.

Note the significant differences when comparing the 1 MW DFD designed using the presented methodology with the 1 MW reference design [11]. Most glaringly, the mass of this DFD is 12.697 times the mass of the reference DFD. As far as the authors are aware, this design is the only one that utilizes scientific scaling relations and ab inito calculations instead of empirical scaling relations and specific powers.

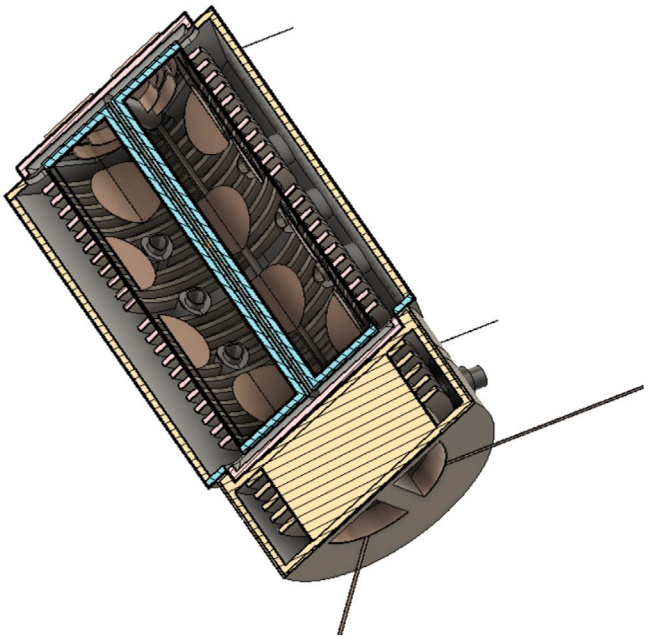

Fig. 12. A view of the Assembled 50 kW DFD. The render does not show the FRC reactor's inner walls, IOT wiring and magnetic nozzle for clarity. The two-fold internal symmetry of the DFD is visible in this image.

Additionally, this work considers the physical material of each DFD component and the materials' physical properties. This novel design approach should account for the discrepancy. Despite the many avenues presented earlier to reduce the mass and improve the design for the next prototype, this work concludes that the total mass target of 1345 kg given in [11] is unrealistic. Considering this design is compliant with international standards, the authors hold that the current reference design does not comply with those same standards, impacting its functionality and precluding its launch aboard a launch vehicle. The analysis here also shows the utility of an MHD generator as the power conversion system's mass fraction is around 8%, approximately a quarter of the previously reported values. The results presented in Table 3 also illustrate the importance of the radial thickness of the HTS double pancake in the flux conservers and the magnetic nozzle on the dimensions and assembled mass of the DFD.

5. Conclusion

The authors addressed the state-of-the-art Field Reversed Configuration (FRC) reactors and research progress into physically realizing the Direct Fusion Drive (DFD). This work identified changes to help reduce the complexity of the DFD and improve its engineering feasibility while considering costs. The changes point to improved FRC stability, plasma confinement, neutron flux magnitudes, and Rotating Magnetic Field (RMF) penetration by including an axial superconducting rod. This work also concluded that solid-state-driven Inductive Output Tubes (IOTs) represent the best technology for powering onboard radio-frequency (RF) systems. Further, it proposed significant changes to the conceptual system architecture of the DFD.

Including a Magnetohydrodynamic (MHD) generator instead of a conventional turbine and radiator system promised reduced complexity, mass, and maintenance requirements on long deep-space missions. It also removed dependence on novel prototype materials and eliminated losses in the fusion output power from waste heat. The work discussed advancements in commercial high-temperature superconducting (HTS) tape and cryostat design to argue that the DFD can significantly reduce its superconductor and neutron shield mass using liquid helium in its cryostat. The last change sought to reengineer the thrust generation mechanism to utilize any one of multiple input propellant options as reaction mass, ensuring reasonable operational costs. The final section detailed the design practices, mathematical scaling relations, and construction materials used to create 50 kW and 1 MW prototypes. It detailed DFD specifications, weight, and design using a parametric CAD. The authors noted that the plasma processor and magnetic nozzle design require further investigation. The results of the design exercise also concluded that the 1 MW reference prototype's mass target is unrealistic. Furthermore, the authors reasoned that the reference design is non-compliant with international design standards for rocket engines and pressure vessels, leading to structural and functional deficiencies and preclusion from launch aboard a launch vehicle.

Declaration of competing interest

The authors declare that they have no known competing financial interests or personal relationships that could have appeared to influence the work reported in this paper.

Data availability

The Fusion 360 Computer-Aided-Design (CAD) files, the COMSOL Multiphysics 6.0 simulation files, and the complete list of calculated parameters are available online with this article.

Acknowledgments

Mr Jain would like to thank ThrustMIT, Manipal, a student-led sounding rocketry team which technically supported this research. Further, Mr Jain expresses his gratitude for various technical discussions and corrections provided by Dr Samuel Cohen of the Princeton Plasma Physics Laboratory (PPPL). Additionally, Mr Jain is thankful for the insight Ms Stephanie Thomas and Mr Yosef S. Razin of Princeton Satellite Systems (PSS) provided on the workings of the Direct Fusion Drive. Finally, Mr Jain would also like to thank Daniel Abraham, Ty Frank, and Naren Shankar for their works, which illustrated the significance of practical nuclear fusion propulsion and assisted him in articulating the potential of the Direct Fusion Drive concept.

Financial statement

This research did not receive any specific grant from funding agencies in the public, commercial, or not-for-profit sectors.

Appendix A. List of acronyms

AC	Alternating Current
AM	Additive Manufacturing
APC	Artificial Flux Pinning
APU	Auxiliary Power Unit
ASME	American Society of Mechanical Engineers
ASTM	American Society for Testing and Materials
BPVC	Boiler and Pressure Vessel Code
CAD	Computer Aided-Design
CVD	Chemical Vapour Deposition
DFD	Direct Fusion Drive
DOE	Department of Energy
EDM	Electrical Discharge Machine
FC	Flux Conserver
FRC	Field Reversed Configuration

HMCF	High Modulus Carbon Fiber
HTS	High-temperature superconductors
ICP	Inductively Coupled Plasma
IOT	Inductive Output Tubes
ISAM	In Space AM
LEO	Low Earth Orbit
LiLFA	Lithium Lorentz Force Accelerator
LTS	Low-temperature superconductors
MHD	Magnetohydrodynamic
MIG	Metal Inert Gas
MLI	Multi-Layer Insulation
NASA	National Aeronautics and Astronautics Administration
NIAC	NASA Innovative Advanced Concept
NPS	Nominal Pipe Standard
OFHC	Oxygen-Free High Thermal Conductivity
PFRC	Princeton Field Reversed Configuration
PFRC - R	Princeton Field Reversed Configuration Reactor
PIC	Particle-In-Cell
RF	Radio Frequency
RMF	Rotating Magnetic Field
SOL	Scrape-Off Layer
TIG	Tungsten Inert Gas
YBCO	Yttrium Barium Copper Oxide

Appendix B. Supplementary data

Supplementary material related to this article can be found online at https://doi.org/10.1016/j.actaastro.2023.02.011.

References

[1] Y.S. Razin, G. Pajer, M. Breton, E. Ham, J. Mueller, M. Paluszek, A.H. Glasser, S.A. Cohen, A direct fusion drive for rocket propulsion, Acta Astronaut. 105 (1) (2014) 145–155.

[2] S.J. Thomas, M. Paluszek, S.A. Cohen, A. Glasser, Nuclear and future flight propulsion-modeling the thrust of the direct fusion drive, in: 2018 AIAA Joint Propulsion Conference, 2018, p. 4769.

[3] S. Cohen, A. Landsman, A. Glasser, Stochastic ion heating in a field-reversed configuration geometry by rotating magnetic fields, Phys. Plasmas 14 (7) (2007) 072508.

[4] L.C. Steinhauer, Review of field-reversed configurations, Phys. Plasmas 18 (7) (2011) 070501.

[5] S. Cohen, B. Berlinger, C. Brunkhorst, A. Brooks, N. Ferraro, D. Lundberg, A. Roach, A. Glasser, Formation of collisionless high-β plasmas by odd-parity rotating magnetic fields, Phys. Rev. Lett. 98 (14) (2007) 145002.

[6] S. Cohen, C. Brunkhorst, A. Glasser, A. Landsman, D. Welch, RF plasma heating in the PFRC-2 device: Motivation, goals and methods, in: AIP Conference Proceedings, Vol. 1406, American Institute of Physics, 2011, pp. 273–276.

[7] S. Cohen, M. Chu-Cheong, R. Feder, K. Griffin, M. Khodak, J. Klabacha, E. Meier, S. Newbury, M. Paluszek, T. Rognlien, et al., Reducing neutron emission from small fusion rocket engines, in: 66th International Astronautical Congress, 2015, pp. 7749–7759.

[8] J.B. Mueller, Y.S. Razin, M.A. Paluszek, A. Knutsen, G. Pajer, S.A. Cohen, A.H. Glasser, Direct fusion drive rocket for asteroid deflection, in: Proceedings, IEPC-2013, Washington, 2013.

[9] S.J. Thomas, M. Paluszek, S. Cohen, N. McGreivy, E. Evans, Fusion-enabled pluto orbiter and lander, in: AIAA SPACE and Astronautics Forum and Exposition, 2017, p. 5276.

[10] M. Paluszek, S. Thomas, Y. Razin, G. Pajer, S. Cohen, Princeton Field Reversed Configuration Reactor for Spacecraft Propulsion, Tech. rep., Princeton Satellite Systems, 2013.

[11] S. Thomas, M. Paluszek, S. Cohen, Fusion-Enabled Pluto Orbiter and Lander: NIAC Phase II Final Report NTRS ID: HQ-E-DAA-TN72513, Tech. rep., Princeton Satellite Systems, 2019.

[12] S. Cohen, C. Swanson, N. Mcgreivy, A. Raja, E. Evans, P. Jandovitz, M. Khodak, G. Pajerj, T. Rognuen, S. Thomas, et al., Direct fusion drive for interstellar exploration, JBIS-J. Br. Interplanet. Soc. 72 (2) (2019) 37–50.

[13] C. Brunkhorst, B. Berlinger, N. Ferraro, S. Cohen, The Princeton FRC rotating-magnetic-field-experiment rf system, in: 2007 IEEE 22nd Symposium on Fusion Engineering, IEEE, 2007, pp. 1–4.

[14] I.R. Jones, A review of rotating magnetic field current drive and the operation of the rotamak as a field-reversed configuration (Rotamak-FRC) and a spherical tokamak (Rotamak-ST), Phys. Plasmas 6 (5) (1999) 1950–1957.

[15] E.S. Evans, S.A. Cohen, D.R. Welch, Particle-in-cell studies of fast-ion slowing-down rates in cool tenuous magnetized plasma, Phys. Plasmas 25 (4) (2018) 042105.

[16] Y. Razin, G. Pajer, M. Breton, E. Ham, J. Mueller, M. Paluszek, A. Glasser, S. Cohen, Modular aneutronic fusion engine, in: Space Propulsion, Citeseer, 2012.

[17] S. Thomas, M. Paluszek, S. Cohen, Fusion-Enabled Pluto Orbiter and Lander: NIAC Phase I Final Report NTRS ID: HQ-E-DAA-TN39262, Tech. rep., Princeton Satellite Systems, 2016.

[18] M. Kim, S. Cohen, S. Thomas, Consideration of vacuum vessel properties required for PFRC-type fusion reactors, in: APS Division of Plasma Physics Meeting Abstracts. Vol. 2021, 2021, pp. JP11–237.

[19] M. Paluszek, G. Pajer, Y. Razin, J. Slonaker, S. Cohen, R. Feder, K. Griffin, M. Walsh, Direct fusion drive for a human Mars orbital mission, in: Proceedings, International Astronautical Congress (AIC) IAC-12, C4, 7-C3. 5, 10, 2014, p. 5064.

[20] C. Swanson, M.A. Paluszek, S. Thomas, Lunar cargo tug using direct fusion drive, in: AIAA Scitech 2021 Forum, 2021, p. 0147.

[21] M. Paluszek, S.J. Thomas, S.A. Cohen, E. Hinterman, Y. Nagai, L. Peng, E. Ham, G. Gaitan, Space nuclear power systems-direct fusion drive, in: 2018 International Energy Conversion Engineering Conference, 2018, p. 4974.

[22] W. Iliffe, N. Peng, G. Brittles, R. Bateman, R. Webb, C. Grovenor, S. Speller, In-situ measurements of the effect of radiation damage on the superconducting properties of coated conductors, Supercond. Sci. Technol. 34 (9) (2021) 09LT01.

[23] K. Tsuchiya, X. Wang, S. Fujita, A. Ichinose, K. Yamada, A. Terashima, A. Kikuchi, Superconducting properties of commercial REBCO-coated conductors with artificial pinning centers, Supercond. Sci. Technol. 34 (10) (2021) 105005.

[24] F. Szecskay, The GE90-designing for maintainability, SAE Trans (1994) 17–23.

[25] B.N. Tomboulian, Lightweight, High-Temperature Radiator for In-Space Nuclear-Electric Power and Propulsion, Tech. rep., University Of Massachusetts Amherst, 2014.

[26] C. Myers, M. Edwards, B. Berlinger, A. Brooks, S. Cohen, Passive superconducting flux conservers for rotating-magnetic-field-driven field-reversed configurations, Fusion Sci. Technol. 61 (1) (2012) 86–103.

[27] J.J. Shang, S.T. Surzhikov, Plasma Dynamics for Aerospace Engineering, Cambridge University Press, 2018.

[28] D.R. Lev, E.Y. Choueiri, Scaling of efficiency with applied magnetic field in magnetoplasmadynamic thrusters, J. Propuls. Power 28 (3) (2012) 609–616.

[29] S.A. Cohen, A.H. Glasser, Ion heating in the field-reversed configuration by rotating magnetic fields near the ion-cyclotron resonance, Phys. Rev. Lett. 85 (24) (2000) 5114.

[30] A.S. Richardson, 2019 NRL Plasma Formulary, Tech. rep., US Naval Research Laboratory, 2019.

[31] J. Glosli, F. Graziani, R. More, M. Murillo, F. Streitz, M. Surh, Molecular dynamic simulations with radiation, J. Phys. A 42 (21) (2009) 214030.

[32] M. Kaushik, L. Joshi, Inductive output tube (IOT)–a review, J. Electromagn. Waves Appl. 29 (15) (2015) 2027–2037.

[33] B.L. Beaudoin, G.S. Nusinovich, G. Milikh, A. Ting, S. Gold, J.A. Karakkad, A.H. Narayan, D.B. Matthew, D.K. Papadopoulos, T.M. Antonsen Jr., Highly efficient, megawatt-class, radio frequency source for mobile ionospheric heaters, J. ElEctromagn. Waves Appl. 31 (17) (2017) 1786–1801.

[34] Communications and Power Industries Inc., CPI VKP-9050 IOT amplifier - Datasheet, 2008, https://www.cpii.com/docs/datasheets/127/VKP-9050%20datasheet.pdf. (Accessed 28 January 2022).

[35] R. Seviour, et al., Comparative Overview of Inductive Output Tubes, ESS Report, June, 2012.

[36] J.M. Woods, C.L. Sercel, T. Gill, B. Jorns, Equivalent circuit model for a rotating magnetic field thruster, in: AIAA Propulsion and Energy 2021 Forum, 2021, p. 3400.

[37] R. Moir, W. Barr, G. Carlson, Direct Conversion of Plasma Energy to Electricity for Mirror Fusion Reactors, Tech. rep., California Univ., 1974.

[38] H. Kobayashi, Y. Okuno, Feasibility study on frozen inert gas plasma MHD generator, IEEE Trans. Plasma Sci. 28 (4) (2000) 1296–1302.

[39] L. Yiwen, L. Yinghong, L. Haoyu, Z. Tao, B. Zhang, C. Feng, Z. Xiaohu, Preliminary experimental investigation on MHD power generation using seeded supersonic argon flow as working fluid, Chin. J. Aeronaut. 24 (6) (2011) 701–708.

[40] B.G. Logan, Inertial fusion reactors using Compact Fusion Advanced Rankine (CFARII) MHD conversion, Fusion Eng. Des. 22 (3) (1993) 151–192.

[41] C.A. Borghi, M. Ishikawa, New concepts of MHD power generation, in: Proc. 12th Int. Conf. MHD Electr. Power Generation. Vol. 1, 1996, pp. 38–46.

[42] R.J. Litchford, N. Harada, Multi-MW Closed Cycle MHD Nuclear Space Power Via Nonequilibrium He/Xe Working Plasma, Tech. rep., NASA Marshall Space Flight Center, 2011.

[43] Tokamac, Wikipedia - Magnetohydrodynamic converter, 2021, https://en.wikipedia.org/wiki/Magnetohydrodynamic_converter#/media/File:MHD_converters_(generator_and_accelerator).svg. (Accessed 15 February 2022).
[44] M. Paluszek, G. Pajer, Y. Razin, J. Slonaker, S. Cohen, R. Feder, K. Griffin, M. Walsh, Direct fusion drive for a human Mars orbital mission, in: Proceedings, International Astronautical Congress (AIC) IAC-12, C4, 7-C3. 5, 10, Princeton Plasma Physics Lab. (PPPL), Princeton, NJ (United States), 2014, p. 5064.
[45] S.J. Thomas, M.A. Paluszek, C. Swanson, Fast human missions to mars using direct fusion drive with a nuclear thermal stage, in: ASCEND 2020, AIAA ASCEND 2020, 2020, p. 4080.
[46] A. Stoneham, J. Matthews, I. Ford, Innovative materials for fusion power plant structures: separating functions, J. Phys.: Condens. Matter 16 (27) (2004) S2597.
[47] N. Baluc, K. Abe, J. Boutard, V. Chernov, E. Diegele, S. Jitsukawa, A. Kimura, R. Klueh, A. Kohyama, R.J. Kurtz, et al., Status of R&D activities on materials for fusion power reactors, Nucl. Fusion 47 (10) (2007) S696.
[48] G. Federici, C.H. Skinner, J.N. Brooks, J.P. Coad, C. Grisolia, A.A. Haasz, A. Hassanein, V. Philipps, C.S. Pitcher, J. Roth, et al., Plasma-material interactions in current tokamaks and their implications for next step fusion reactors, Nucl. Fusion 41 (12) (2001) 1967.
[49] V. Livramento, D. Nunes, J. Correia, P. Carvalho, U. Mardolcar, R. Mateus, K. Hanada, N. Shohoji, H. Fernandes, C. Silva, et al., Tungsten–microdiamond composites for plasma facing components, J. Nucl. Mater. 416 (1–2) (2011) 45–48.
[50] J. Knaster, A. Moeslang, T. Muroga, Materials research for fusion, Nat. Phys. 12 (5) (2016) 424–434.
[51] D. Park, J. Bascuñán, Y. Li, W. Lee, Y. Choi, Y. Iwasa, Design overview of the MIT 1.3-GHz LTS/HTS NMR magnet with a new REBCO insert, IEEE Trans. Appl. Supercond. 31 (5) (2021) 1–6.
[52] C. Senatore, C. Barth, M. Bonura, M. Kulich, G. Mondonico, Field and temperature scaling of the critical current density in commercial REBCO coated conductors, Supercond. Sci. Technol. 29 (1) (2015) 014002.
[53] D. Uglietti, A review of commercial high temperature superconducting materials for large magnets: from wires and tapes to cables and conductors, Supercond. Sci. Technol. 32 (5) (2019) 053001.
[54] W. Han, X. Qian, H. Ma, X. Wang, Y. Zhang, Effect of nickel electroplating followed by a further copper electroplating on the micro-structure and mechanical properties of high modulus carbon fibers, Mater. Today Commun. 27 (2021) 102345.
[55] T.Q. Tran, J.K.Y. Lee, A. Chinnappan, N.H. Loc, L.T. Tran, D. Ji, W. Jayathilaka, V.V. Kumar, S. Ramakrishna, High-performance carbon fiber/gold/copper composite wires for lightweight electrical cables, J. Mater. Sci. Technol. 42 (2020) 46–53.
[56] A. Kogan, J. Fesmire, W. Johnson, J. Minnick, Cryogenic Vacuum Insulation for Vessels and Piping, Tech. rep., NASA Kennedy Space Center, 2010.
[57] P.T. Finley, R.A. Hopkins, R.B. Schweickart, Flight cooling performance of the Spitzer Space Telescope cryogenic telescope assembly, in: Optical, Infrared, and Millimeter Space Telescopes. Vol. 5487, SPIE, 2004, pp. 26–37.
[58] M. Hirabayashi, K. Narasaki, S. Tsunematsu, Y. Kimura, S. Yoshida, H. Murakami, T. Nakagawa, A. Ohnishi, T. Matsumoto, H. Kaneda, et al., Thermal design and its on-orbit performance of the AKARI cryostat, Cryogenics 48 (5–6) (2008) 189–197.
[59] D. Glaister, J. Schmidt, C. McLean, G. Mills, Long term cryogenic storage technologies overview for NASA exploration applications, in: 42nd AIAA Thermophysics Conference, 2011, p. 3774.
[60] Cambridge Isotope Laboratories, Deuterium (d, 99.8%) chemical purity 99.999%, 2020, https://shop.isotope.com/productdetails.aspx?itemno=DLM-408-HP-PK. (Accessed 03 February 2022).
[61] National Aeronautics and Astronautics Administration, Space shuttle super lightweight external tank - Factsheet, 2008, http://www.nasa-klass.com/Curriculum/Get_Training%201/ET/RDG_ET-Additional/SuperLightweightTank.pdf. (Accessed 06 February 2022).
[62] S. Dillich, T. Ramsden, M. Melaina, Hydrogen production cost using low-cost natural gas, DOE Hydrogen and Fuel Cells Program Record 12024 (2012).
[63] A.J. Sheppard, J.M. Little, Scaling laws for electrodeless plasma propulsion with water vapor propellant, Plasma Sources. Sci. Technol. 29 (4) (2020) 045007.
[64] A. Kodys, E. Choueiri, A critical review of the state-of-the-art in the performance of applied-field magnetoplasmadynamic thrusters, in: 41st AIAA/ASME/SAE/ASEE Joint Propulsion Conference & Exhibit, 2005, p. 4247.
[65] B.D. Solomon, K. Krishna, The coming sustainable energy transition: History, strategies, and outlook, Energy Policy 39 (11) (2011) 7422–7431.
[66] NXP Semiconductors Inc., MRFX1K80H LDMOS power RF transistor - datasheet, 2018, https://www.nxp.com/docs/en/data-sheet/MRFX1K80H.pdf. (Accessed 06 February 2022).
[67] PileupDX.com, OM4001A HF 4KW automatic amplifier, 2021, https://pileupdx.com/product/om4001a-hf-4kw-automatic-amplifier/. (Accessed 06 February 2022).
[68] J. Joseph, G. Agrawal, D.K. Agarwal, J. Pisharady, S.S. Kumar, Effect of insulation thickness on pressure evolution and thermal stratification in a cryogenic tank, Appl. Therm. Eng. 111 (2017) 1629–1639.
[69] D.S. Sharma, Stress distribution around polygonal holes, Int. J. Mech. Sci. 65 (1) (2012) 115–124.
[70] SpaceX, Falcon payload user's guide - SpaceX, 2021, https://www.spacex.com/media/falcon_users_guide_042020.pdf. (Accessed 10 January 2023).
[71] CIS GmbH Consulting Inspection Services, ASME BPVC allowable stress tables - non-ferrous materials, 2021, https://www.cis-inspector.com/asme-code-allowable-stresses-table-1b.htm. (Accessed 10 January 2023).
[72] F.R. Schwartzberg, S. Osgood, R. Keys, Cryogenic Materials Data Handbook, Tech. rep., Martin Co denver Co, 1963.
[73] M. Fink, T. Fabing, M. Scheerer, E. Semerad, B. Dunn, Measurement of mechanical properties of electronic materials at temperatures down to 4.2 K, Cryogenics 48 (11–12) (2008) 497–510.
[74] K.-P. Weiss, N. Bagrets, C. Lange, W. Goldacker, J. Wohlgemuth, Thermal and mechanical properties of selected 3D printed thermoplastics in the cryogenic temperature regime, IOP Conf. Ser. Mater. Sci. Eng. 102 (2015) 012022.
[75] K. Nogi, Y. Aoki, H. Fujii, K. Nakata, S. Kaihara, Weld formation in microgravity, ISIJ Int. 38 (2) (1998) 163–170.
[76] B. Thomas, A. Atkinson, R. Dashwood, Strength of soldered joints formed under microgravity conditions, J. Electron. Mater. 36 (1) (2007) 1–5.
[77] N. Leach, 3D printing in space, Archit. Des. 84 (6) (2014) 108–113.
[78] E. Sacco, S.K. Moon, Additive manufacturing for space: status and promises, Int. J. Adv. Manuf. Technol. 105 (10) (2019) 4123–4146.
[79] H. Gu, L. Li, Computational fluid dynamic simulation of gravity and pressure effects in laser metal deposition for potential additive manufacturing in space, Int. J. Heat Mass Transfer 140 (2019) 51–65.
[80] S. Rawal, J. Brantley, N. Karabudak, Additive manufacturing of Ti-6Al-4V alloy components for spacecraft applications, in: 2013 6th International Conference on Recent Advances in Space Technologies, RAST, IEEE, 2013, pp. 5–11.
[81] H. Habazaki, T. Onodera, K. Fushimi, H. Konno, K. Toyotake, Spark anodizing of β-Ti alloy for wear-resistant coating, Surf. Coat. Technol. 201 (21) (2007) 8730–8737.
[82] A. Miller, G.D. Barnett, Chemical vapor deposition of tungsten at low pressure, J. Electrochem. Soc. 109 (10) (1962) 973.
[83] K. Sankaran, E. Choueiri, S. Jardin, Investigation of Basic Processes in a Lithium Lorentz Force Accelerator Through Plasma Flow Simulation, Electric Propulsion and Plasma Dynamics Laboratory, Princeton Univ., Princeton, NJ, 2005.
[84] A. Shiri, A. Shoulaie, Calculation of the magnetic forces between planar spiral coils using concentric rings, ACES J. Appl. Comput. Electromagn. Soc. 25 (5) (2010) 468.
[85] IPC - 2221, PCB trace width calculator, 1998, https://www.4pcb.com/trace-width-calculator.html. (Accessed 03 February 2022).
[86] Haynes International, Hastelloy C-276 alloy, 2022, https://www.haynesintl.com/alloys/alloy-portfolio_/Corrosion-resistant-Alloys/HASTELLOY-C-276-Alloy/physical-properties. (Accessed 10 January 2023).
[87] S. Iwai, M. Takahashi, H. Miyazaki, T. Tosaka, K. Tasaki, S. Hanai, S. Ioka, K. Watanabe, S. Awaji, H. Oguro, Design of a cooling system for a REBCO insert coil in a cryogen-free 25 T superconducting magnet, IEEE Trans. Appl. Supercond. 25 (3) (2014) 1–4.